Available online at www.sciencedirect.com
ScienceDirect
Ceramics International 36 (2010) 263–274
CERAMICS INTERNATIONAL
www.elsevier.com/locate/ceramint

The influence of microstructure on the maximum load and fracture energy of refractory castables

S. Ribeiro [a,*], J.A. Rodrigues [b]

[a] Materials Engineering Department, School of Engineering of Lorena, University of São Paulo, 12600-970, Lorena, SP, Brazil
[b] Materials Engineering Department, Federal University of São Carlos, 13565-905, São Carlos, SP, Brazil

Received 13 January 2009; received in revised form 14 June 2009; accepted 26 July 2009
Available online 27 August 2009

Abstract

Refractory castables are composed of fractions of fine to fairly coarse particles. The fine fraction is constituted primarily of raw materials and calcium aluminate cement, which becomes hydrated, forming chemical bonds that stiffen the concrete during the curing process. The present study focused on an evaluation of several characteristics of two refractory castables with similar chemical compositions but containing aggregates of different sizes. The features evaluated were the maximum load, the fracture energy, and the ''relative crack-propagation work'' of the two castables heat-treated at 110, 650, 1100 and 1550 °C. The results enabled us to draw the following conclusions: the heat treatment temperature exerts a significant influence on the matrix/aggregate interaction, different microstructures form in the castables with temperature, and a relationship was noted between the maximum load and the fracture energy.

Keywords: Refractory castable; Microstructure; Fracture energy; Wedge splitting method

1. Introduction

1.1. Refractories—definition and history

Refractories are materials with complex and coarse microstructures consisting of a population of very coarse particles called aggregates (in the order of millimeters in size) and a fine fraction (which can be as fine as nanometric in size), called the matrix, which interlinks the coarser particles of the material. The fine fraction promotes the chemical bond formation at low temperature (through the formation of hydrates which are responsible for the stiffness of the material) and ceramic bond formation at high temperature (dehydratation, followed by sintering of the particles). Refractories are frequently applied in processes involving high temperatures and aggressive environments subject to thermal shocks and corrosion, as in the production of metals, glasses, cements and oil derivatives [1,2].

Initially, refractories were used in the form of bricks for furnace lining. In 1914, a new form of lining was presented commercially, leading to the emergence of the so-called monoliths, whereby a fluid mass of refractory aggregate was placed inside the furnace, forming an entire seamless wall, which made the application of these materials far more efficient. These materials are the so-called refractory castables [1].

1.2. Cure and hydratation of the refractories

Refractory castables are complex formulations, requiring high quality raw materials, precise control aggregate sizes, additives, and binders [1]. Basically, refractory castables are produced by the mixture of calcium aluminate cement (CAC), certain fine raw materials, aggregates, additives, and water.

After mixing the solid raw materials (cement, aggregate and fine particles), water is added, causing the phenomenon of hydration; and forming a stiff structure in the green concrete, which will indirectly influence the castable properties after firing. Several phases can be formed during hydration, with distinct chemical and mineralogical compositions. The material formed has different relative quantities that depend on several

* Corresponding author. Tel.: +55 12 31599913; fax: +55 12 31533006.
E-mail address: sebastiao@demar.eel.usp.br (S. Ribeiro).

0272-8842/$36.00
doi:10.1016/j.ceramint.2009.07.033

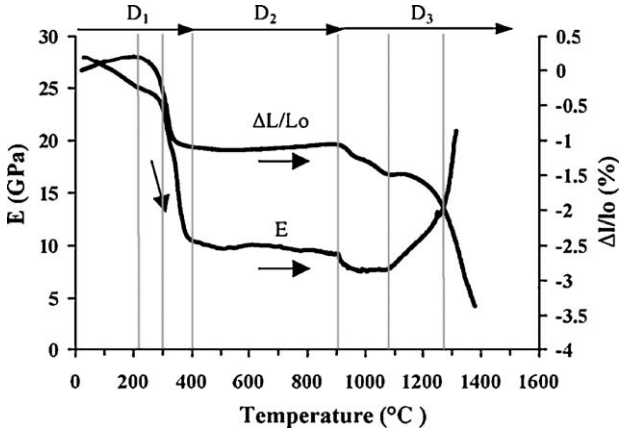

Fig. 1. Variation of Young's modulus, E, and of the relative dimension, $\Delta L/L_0$, as a function of the heat treatment temperature of a cement and water paste [2].

factors, e.g., curing temperature, CaO/Al_2O_3 (C/A) ratio, the amount of water, and the presence of impurities both in the aluminate solution, and on the surface of the aggregates and other raw materials [1,2].

After curing, a refractory castable is subjected to high temperature processing and usage; which, depending on the temperature attained, causes alterations of the phases during curing of the castables, as well as variation of its chemical composition. The chemical composition of a castable varies, particularly with respect to water, since the refractory castable dehydrates during heating. These variations lead to microstructural changes that may improve or reduce the refractory's mechanical strength, and lead to variations in its density, pore distribution, and pore size.

When refractory castables or pastes containing CAC are heat-treated, they undergo microstructural modifications that lead to a change in their mechanical behavior. Research has shown that when these materials are heated between 200 and 300 °C, their mechanical strength is diminished in relation to the material that is only cured, which contributes to an increase in porosity caused by the loss of water of hydration. Fig. 1 shows the variation in Young's modulus and in the dimension of samples prepared using 100 g of cement and 33 g of water, standardizing as a water-to-cement ratio of 0.33. The chemical composition of the cement is: CaO = 27.00, Al_2O_3 = 60.72, Na_2O = 0.25, SiO_2 = 0.30, Fe_2O_3 = 0.15, MgO = 0.20, wt%, with a specific surface area of 1.66 $m^2\ g^{-1}$, and with a bulk density of 3.04 g cm^{-3} [2]. Note that, starting at about 1100 °C, there is a visible recovery of Young's modulus, which is attributed to the beginning of the formation of ceramic bonds (sintering), and to the reduction of porosity, both change causing an increase in the mechanical strength of the material [2–5]. It is well known that Young's modulus is influenced by porosity [6]. In addition to porosity, Young's modulus is also affected by the cohesion among the particles of the material. That is why this modulus declines when the hydrates are destroyed, and later recovers through sintering [6–9].

Fig. 2 depicts the microstructures of the composition using 79.00 wt% of Al_2O_3 (99.80 wt% Al_2O_3 purity) and 21.00 wt% of cement (the chemical composition of this cement was cited early) [2]. The samples of this composition were prepared using a water/cement ratio of 0.91, afterwards materials were than dried and sintered at 1300 or 1550 °C for 2 h, using heating/cooling rates of 5 °C/min [2]. These micrographs show typical globular crystals morphologies of CA_2 ($CaO{\cdot}2Al_2O_3$) (Fig. 2(a)); and a hexagonal morphology of the CA_6 ($CaO{\cdot}6Al_2O_3$) grains (Fig. 2(b)), indicating the microstructural evolution from the specific heat treatment temperature procedure [2].

Fig. 3 shows a complete view of the entire process of hydration, dehydration and sintering of an alumina-based refractory castable containing CAC, indicating the regions of temperature where phase formation and transformation occur [10]. The upper part of the figure shows the cement, presenting the phases CA ($CaO{\cdot}Al_2O_3$), CA_2, $C_{12}A_7$ ($12CaO{\cdot}7Al_2O_3$) in the presence of water (H); and the alumina aggregates (Tabular grog). When in contact with water, these phases hydrate, and transform into various hydrates whose crystalline structures depend on the temperature, as indicated in Fig. 3, between 20 and 350 °C. The phases are symbolized by AH_3 and CAH_{10}, C_2AH_8 and C_3AH_6, which represent $Al_2O_3{\cdot}3H_2O$ [or $Al(OH)_3$], $CaO{\cdot}Al_2O_3{\cdot}10H_2O$, $2CaO{\cdot}Al_2O_3{\cdot}8H_2O$ and $3CaO{\cdot}Al_2O_3{\cdot}6H_2O$, respectively. When the temperature increases, these hydrates decompose, forming A,

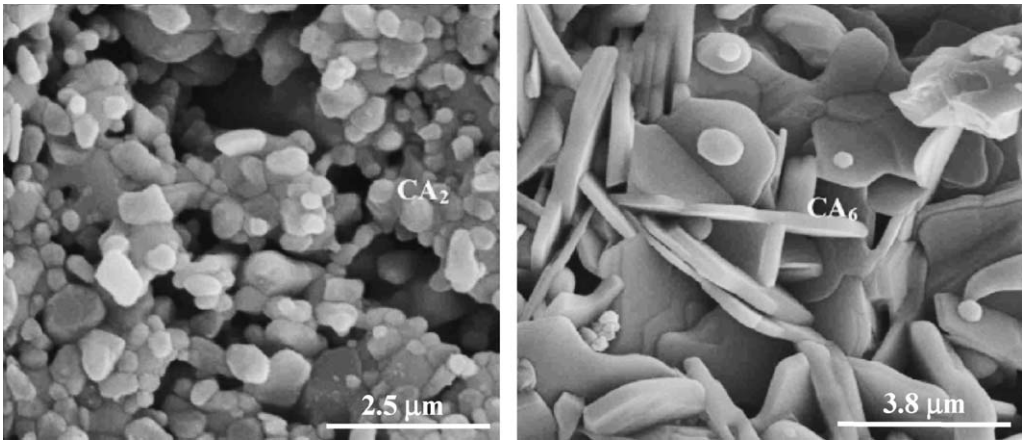

Fig. 2. SEM micrographs of fracture surfaces of samples prepared using $CaO–Al_2O_3$: (a) sintered at 1300 °C and (b) sintered at 1550° C for 2 h, showing the evolution and morphology of CA_2 and CA_6, respectively [2].

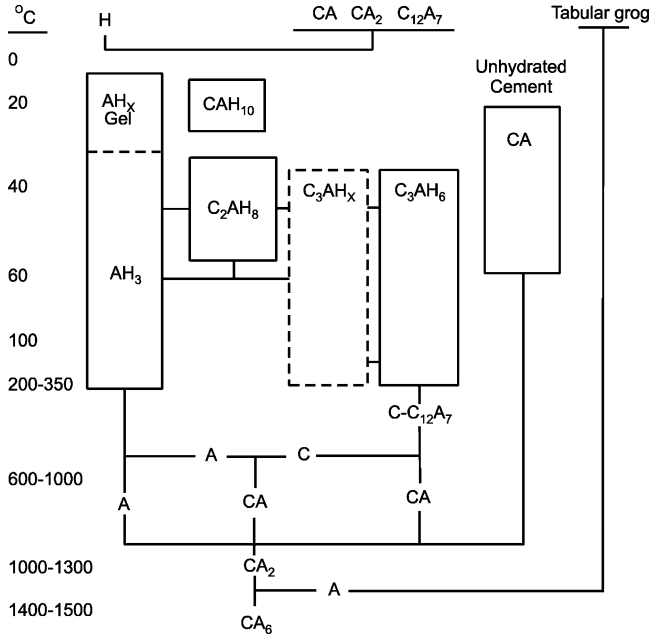

Fig. 3. Transformations that can occur during the heating of alumina refractory castables containing CAC [10].

C (CaO), $C_{12}A_7$, CA, CA_2 and even CA_6, depending on the amount and reactivity of the alumina initially present [10].

A comparison can be made of the micrographs of Fig. 2(a and b) and the lower part of Fig. 3, which indicates the formation of CA_2 and CA_6 phases observed at temperatures of 1300 and 1550 °C, respectively. Simonin et al. showed using X-ray diffraction analyses that above 600 °C no hydrates existed with the crystallized phases formed, having a mineralogical structure dependent on the final temperature to which a material was exposed [4].

1.3. Thermal shock

Once a refractory was made and processed, it was characterized for mechanical and thermomechanical properties, with one of the most important properties being thermal shock damage resistance, since these materials normally are used in severe conditions of temperature cycling and of temperature differences along a body. To study the thermal shock damage of refractories, two parameters were presented by Hasselman and mathematically expressed in the following equations [11–19]:

$$R''' = \frac{\gamma_{wof} E}{\sigma_f^2 (1-\nu)} \quad (1)$$

$$R_{st} = \left[\frac{\gamma_{wof}(1-\nu^2)}{E\alpha^2}\right]^{1/2}, \quad (2)$$

where R''' is the parameter of thermal shock damage resistance, R_{st} is the parameter of crack stability under thermal stress, ν is the Poisson's ratio, σ_f is the modulus of rupture, α is the coefficient of linear thermal expansion, and γ_{wof} is the fracture energy.

As can be seen, fracture energy is an important term in the prediction of the thermal shock damage resistance of a refractory material. Applying the equations to a refractory, the results can be used to design new materials, or to improve those already commercially available on the market.

1.4. Fracture energy

Fracture energy can be defined as the mean work per unit of projected fracture area required to propagate a stable crack, and is represented by the sum of distinct energies consumed during the crack propagation process. The value of γ_{wof} can be determined from the load–displacement curve obtained from stable crack propagation tests and from the following equation [11,15,18–21]:

$$\gamma_{wof} = \frac{1}{2A}\int P_M d\delta \quad (3)$$

where A is the projected area of the fracture surface, P_M is the vertical load applied by the testing machine, and δ is the displacement of the machine's actuator. The value of the integral in Eq. (3) is determined by the total area under the corresponding load–displacement curve.

Fig. 4 illustrates a typical load–displacement curve obtained during a crack propagation test by the wedge splitting method, a test which will be used to determine the fracture energy of the commercial refractory castables in this study. This curve reveals stable crack propagation, mainly near the maximum load, of the crack throughout the test. The operational conditions of the mechanical tests used to obtain this curve were: load cell of 5 kN, test control by actuator displacement, and ramp-up of 0.020 mm min^{-1} (3.33×10^{-7} m s^{-1}). The attained maximum load (P_{max}) is observed in Fig. 4.

The area under this curve can be divided into three distinct regions: "*A*", "*B*" and "*C*". Region "*A*" is characterized by a linear elastic behavior. In region "*B*", between the end of the linear region (point a in Fig. 4) and the point of maximum load (P_{max}), the graph shows a curve which indicates the beginning of the growth of the crack (starting from the tip of the notch),

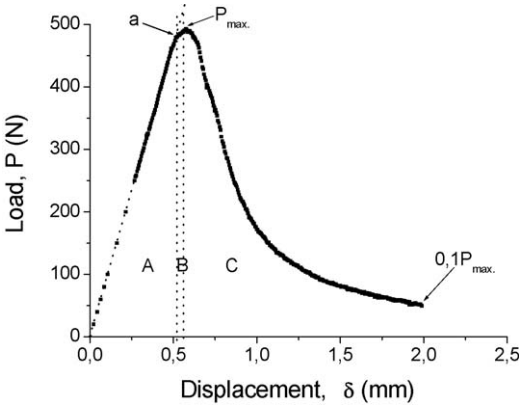

Fig. 4. Load–displacement curve typical of one of the refractory castables of this work, in the stable crack propagation test by the wedge splitting method.

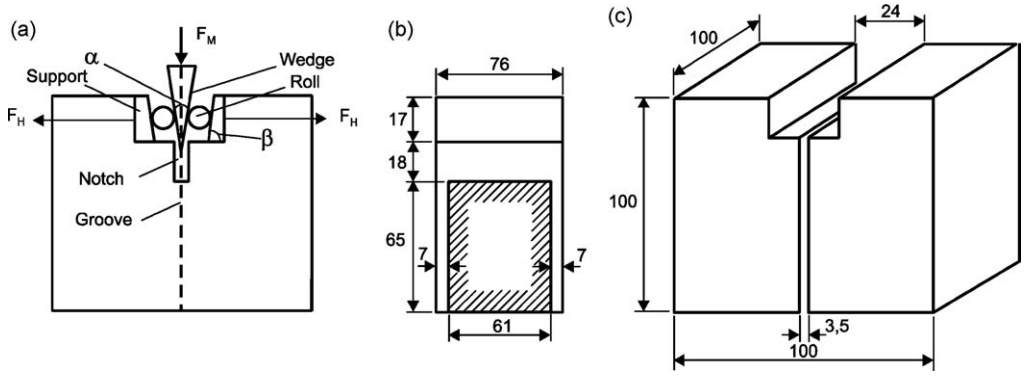

Fig. 5. (a) The test fixture and sample dimensions (all dimensions in mm) for the wedge splitting test [16,17,32], (b) cross-section of the sample, passing through the notch and lateral grooves [17], and (c) geometry and dimensions of the sample; all measures in mm.

along with increasing load, until a critical size is reached at the highest load point of the curve (P_{max}). This size is called ''critical crack length'' [20,22]. Region ''*C*'' is characterized by continuous and stable propagation of the crack as the load decreases.

The profile of the curve in Fig. 4 and the corresponding value of fracture energy depend on several factors, which include the strength of the matrix, the matrix–aggregate interfacial interaction, and the size and tensile strength of the aggregates. Toughening mechanisms acting in the microstructure will also influence the fracture energy. The strength of the matrix–aggregate interface can be evaluated by the fracturing of aggregates when the test specimen is subjected to quasi-static crack opening test [20,23]. Depending on these properties, the three regions of the load–displacement curve vary in different materials. These differences can be evaluated by relating those areas to each other, mainly those referring to the energy stored in region *A* and the region of stable crack propagation, *C*.

The study of the relationships between areas ''*A*'', ''*B*'' and ''*C*'' can be used to evaluate the fracture behavior of mortars and castables. This is done by evaluating $[(B + C)/A]$ [23,24]. The value of this relation can be highly dependent on the properties of the matrix–aggregate interface, and this can be correlated with the fracturing or nonfracturing of the aggregates in the matrix. If the aggregates are tightly bonded in the matrix, they may undergo greater fracturing, or if loosely bond, the aggregates are pulled out from the matrix during stable crack propagation, eventually causing interlocking of the two fracture surfaces. This has the effect of increasing the fracture energy, reaching to a higher resistance against the crack propagation, which caused an increase of the $[(B + C)/(A)]$ ratio [25–28]. Different authors have studied this behavior of refractories using the ratios between the ''*A*'', ''*B*'' and ''*C*'' areas, calling it flexibility [24], or the flexibility ratio. In the present work, we call the $[(B + C)/(A)]$ ratio ''relative crack-propagation work'', since we consider it a better way to describe the behavior of crack propagation. This ratio, thus defined, considers all the work in the effective crack propagation (including the subcritical region ''*B*'') in relation to solely elastic work. Therefore, the higher this relative work, the more resistant the material would be to the propagation of a crack.

Fracture energy in prismatic samples can be determined experimentally by three-point bending. However, a more recent and widely accepted test, which has been used frequently for materials with coarse microstructures, is the method patented by Tschegg under the name ''*Wedge Splitting Test*'' [29,30]. This method, which consists of opening a crack using a wedge, can be called simply the ''Wedge Method''. This technique is being used by a numerous research centers and universities, as well as by manufacturers of refractories [16,26,29,31–33]. Fig. 5(a) illustrates how the components are used in this method. As can be seen in the figure, the wedge receives the load from the machine, F_M, and transmits a load to the lateral rolls, and from these to the supports; which produce the horizontal forces, F_H, causing opening of the crack (notch), and its subsequent propagation. Fig. 5(b) shows details of the notch, the lateral grooves and the fractured section after the test. Fig. 5(c) depicts the geometry of the sample and its typical dimensions (in mm) [16,17].

The main advantage of the wedge test is the possibility of working with relatively large samples, for which the size of the aggregate is sufficiently small in relation to the cross-section area, which results in a low ratio of aggregate/transversal dimensions. In the wedge test, the force applied by the testing machine is quite small due to the wedge effect. The wedge effect can be analyzed by the following equation [16,17,31,32]:

$$F_H = \frac{F_M}{2\tan(\alpha/2)}, \tag{4}$$

where α is the angle of the wedge (smaller α, bigger F_H/F_M ratio) and F_H is the horizontal force produced by F_M, which is the vertical load applied by the testing machine. Since $F_H > F_M$, this reduces the load applied on the machine's frame, storing less elastic energy in it, thus reducing the possibility of instability during crack propagation through a sudden release of energy.

The objective of the present work was to study the behavior of two commercial refractory castables with similar chemical compositions but having aggregates of different particles sizes. To this end, maximum load, fracture energy and the ''relative

Table 1
Chemical composition and apparent density of the castables used in this work (data given by the supplier).

Castable	Chemical composition (wt%)				
	Al_2O_3	CaO	$Na_2O + K_2O$ (maximum)	SiO_2 (maximum)	Fe_2O_3 (maximum)
A	94.00/98.00	3.00/4.00	0.40	0.30	0.08
B	95.00/98.00	2.00/3.50	Trace	Trace	Trace

crack-propagation work'' were determined from load–displacement curves. The results from those curves were correlated with the microstructure of the two materials under study.

2. Materials and methods

2.1. Raw materials and its characteristics

Two commercial alumina-based refractories were used, identified here as *A* and *B*. Tables 1 and 2 show the chemical composition (given by the supplier) and particles size and its amounts, respectively, of the two castables. In Table 2 can be seen the difference between the particles sizes in the two concretes. The finer fractions (smaller than 0.0108 mm) constitute the matrix of the two refractory castables, and its compositions are cement (2 wt% in both concretes) and reactive alumina. The coarse fractions (above 0.0108 mm) are composed of Al_2O_3 aggregate in both concretes, comprising 64.36 and 67.8 wt% of aggregates in *A* and *B* castables, respectively.

2.2. Preparation of the samples

To produce the test specimens of concrete *A*, were used 2200.0 g of raw materials (cement, reactive alumina and aggregates) and 209.0 g of water, which is equivalent to 9.5 wt% of water relative to the solid mass. For concrete *B*, 2200.0 g of solids and 187.0 g of water were used, equivalent to 8.5 wt% of the solid mass. These water quantities produced a mass with good consistency for molding. The materials were mixed for 2 min in a planetary mixer prior to casting.

Table 2
Particle size and distribution particles size of the two concretes obtained by sieves analysis.

Aperture size (mm)	wt% retained	
	A	*B*
+22.43	0.00	0.00
−22.43 + 9.5	0.00	8.97
−9.5 + 4.75	0.24	19.35
−4.75 + 2.00	17.55	19.55
−2.00 + 0.85	27.16	7.11
−0.85 + 0.6	2.98	2.70
−0.60 + 0.425	10.98	5.95
−0.425 + 0.30	3.59	3.23
−0.30 + 0.212	0.50	0.76
−0.212 + 0.125	0.48	0.09
−0.125 + 0.108	0.88	0.09
−0.0108	35.64	32.20

After mixing, the castables were poured into a PVC mold equipped with steel blades that produced the grooves and the notch on the test specimens. Fig. 6 shows a photograph of the mold with its steel blades. A vibrating table was used to help settle the concrete in the mold and remove entrapped air. The notch produced in this way is of the ''V''-type, with an angle equal to 60°. This increases the stress concentration at the notch tip facilitating the initial stable propagation of the crack.

The test specimens were cured at 23 °C for 48 h in a water-saturated atmosphere. The samples were removed from the mold 24 h after curing started. All the test specimens were then oven-dried at 110 °C for 48 h. After curing and drying, groups of test specimens were subjected to distinct heat treatments in preparation for evaluating their respective properties as a function of the microstructure induced in them. One microstructural condition resulted from the curing and drying of the material, with other microstructures produced by different 12 h heat treatments applied to groups of samples at: 650, 1100 and 1550 °C. The heating rate used to reach the soak temperature was 2 °C/min, and a cooling rate to reach the room temperature was 1 °C/min. Four distinct microstructural conditions were produced, namely, from the purely green (cured and dried) to the sintered material. To align the test specimens within the testing machine, they were all ground at their respective bases by a diamond grinding wheel with grains size average 80 μm.

2.3. Apparent density and apparent porosity

Apparent density and apparent porosity of prepared specific samples were determined by the water immersion method according DIN 51056.

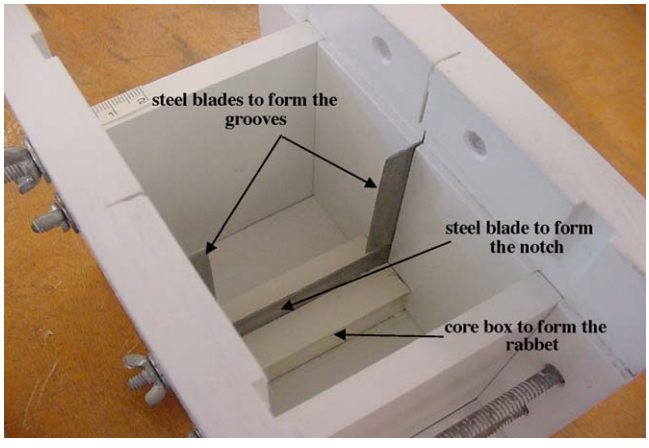

Fig. 6. Photograph of the PCV mold, showing the steel blades to form the notch and the grooves on the test specimen during molding.

2.4. Stable crack propagation

To carry out the stable crack propagation tests, the specimens were placed in an appropriate holder together with the device containing the supports, the rolls and the wedge. The set was mounted on an MTS model 810 mechanical testing machine (Material Testing System) using a TestStar IIs controller. In this work, a wedge with α-angle equal 10° and supports with β-angle equal to 5° (see Fig. 5(a)) were used, with a horizontally transmitted load, F_H, 5.7 times greater than the load applied by the machine, F_M. The operational conditions of the mechanical tests were: load cell of 5 kN, test control by actuator displacement, and ramp-up of $0.020\,\text{mm}\,\text{min}^{-1}$ ($0.333 \times 10^{-6}\,\text{m}\,\text{s}^{-1}$). The γ_{wof} values were obtained through the integral of the $F_M \times \delta$-curves for the δ-values from zero up to the displacement corresponding to 10% of $P_{\max}$, after the maximum load point that was reached in the test. The wedge splitting tests were performed at room temperature.

2.5. Microstructural analysis

The fracture surfaces obtained in the crack propagation tests of the samples of refractories *A* and *B* were analyzed by scanning electron microscopy (SEM) to determine possible microstructural variations and their influence on the properties studied here. The samples were coated with a gold film to render them conductive, and the secondary electron (SE) mode was used.

2.6. Count of fractured aggregates

The purpose of making a semi-quantitative evaluation of fractured aggregates in the samples of refractories *A* and *B* that were heat-treated at 110, 650, 1100 and 1550 °C was to obtain data for comparison with maximum load, fracture energy and relative crack-propagation work. Microstructure date was used to compare samples of the same refractory subjected to different heat treatment temperatures. To correlate the results of the two refractories would require counting all the aggregates of the samples and obtaining a relation between fractured and total aggregates, which was not determined in this study. To carry out the aggregates count, two samples from each heat treatment temperature were used, which were selected as a function of the fracture energy results. The fracture surfaces evaluated were taken from one of the test specimens that were subjected to stable crack propagation testing.

3. Results and discussion

3.1. Apparent density and apparent porosity

Table 3 shows the apparent density and porosity results of samples from castables *A* and *B* dried at 110 °C (110A and 110B), calcined at 650° (650A and 650B), and sintered at 1100 °C (1100A and 1100B) or 1550 °C (1550A and 1550B).

In this table, it is noted that the apparent densities are similar for all temperatures and refractory castable compositions (*A* and *B*), except at 1550 °C, which had lower values. Following the same tendency, the porosities are similar, with a small decrease as temperature increase in the *A* composition, but with significant increase for samples sintered at 1550 °C. The cause of this increase was assumed to be the high sintering temperature caused the evaporation of some substance during soaking time (1550 °C for 12 h), which produced higher porosity and lower density than other heat treatment temperatures. The different quantities of the water added in concrete *A* (9.5 wt%) and concrete *B* (8.5 wt%) are not enough to negatively influence the densities and apparent porosities in concrete *A*, so concrete *B* had more consistent porosity values at lower temperatures.

Table 3
Apparent density and porosity of the samples from castables *A* and *B* dried at 110 °C (110A and 110B), calcined at 650 °C (650A and 650B), and sintered at 1100 °C (1100A and 1100B) and 1550 °C (1550A and 1550B).

Sample	Apparent density (g/cm^3)	Porosity (%)
110A	2.92 ± 0.06	16.69 ± 1.06
650A	2.98 ± 0.05	16.33 ± 0.96
1100A	2.99 ± 0.05	15.79 ± 0.92
1550A	2.82 ± 0.06	25.70 ± 1.09
110B	2.99 ± 0.07	13.24 ± 1.06
650B	2.96 ± 0.05	13.59 ± 1.01
1100B	2.98 ± 0.06	13.48 ± 0.86
1550B	2.80 ± 0.05	23.94 ± 1.06

3.2. Stable crack propagation

Fig. 4, as mentioned, depicts a load–displacement curve of refractory *A* cured for 48 h under controlled humidity conditions, then dried at 110 °C for 48 h. It showed the three distinct regions. The maximum load indicates mechanical strength under a condition of slow crack propagation, contrary to the notion of modulus of rupture under a condition of catastrophic fracture. In the slow crack growth of the wedge test, one can monitor the transformation of elastic energy stored in the test specimen and in the machine into surface energy and into energy consumed by dissipation during the quasi-static crack propagation.

3.3. Maximum load

Fig. 7 illustrates the behavior of refractories *A* and *B* with respect to maximum load. The graphs in the figure indicate that the heat treatment temperature influences the maximum load in both refractories, with bigger difference for sample *B* sintered at 1550 °C. This indicates that the aggregate contributes strongly to the material microstructure, and, hence, to the final properties of material. The aggregates of concrete *B* had a different size distribution and larger size of particles than material *A* (see Table 2).

For both the refractories, the maximum load increased with heat treatment temperature, except at 650 °C, where it decreased sharply. The explanation for this behavior is in the

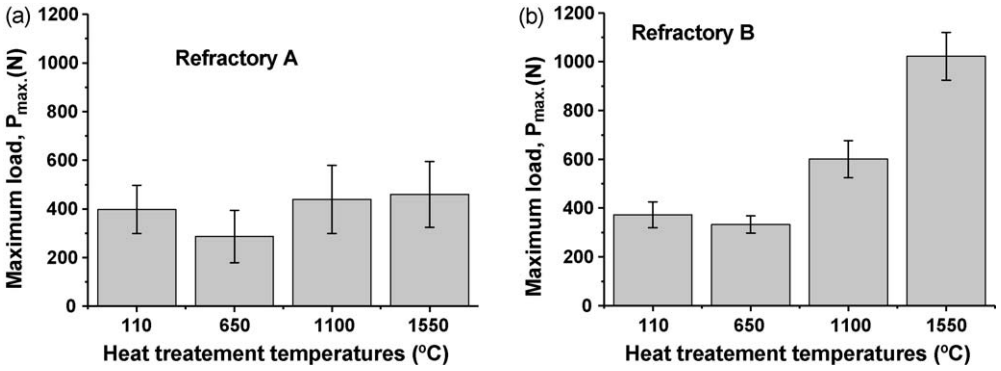

Fig. 7. Maximum load graphs of the samples of refractory castables "*A*" (a) and "*B*" (b), heat-treated at different temperatures as indicated under the respective horizontal axes.

microstructure, because at 110 °C the concrete is cohesive due to the formation of hydrates during curing, which provides a rigid interaction inside the matrix and between the matrix and the aggregates. When these castables were fired at 650 °C, the hydrates formed at the low temperatures were destroyed, causing a strength reduction in the two concretes. This behavior can be compared with that depicted in Fig. 1, where the modulus of elasticity decreases in the temperature region around 650 °C, indicating a loss of cohesion in the material structure [2]. When the test specimens were fired at 1100 °C, another mechanism of bonding began between the constituents of the refractory grains, i.e., the beginning of the formation of ceramic bonds by sintering. This helps to explain why Fig. 7 shows a visible recovery in the maximum load. The maximum load was greatest at 1550 °C, when sintering of the refractories was greatest.

3.4. Microstructure

Important aspects of the microstructural changes resulting from the four heat treatment temperatures are depicted in the micrographs of Fig. 8, for material *A*, and in Fig. 9 for material *B*. Figs. 8(a) and 9(a) show microstructures that consist of interlinked particles of hydrates that bond the matrix and

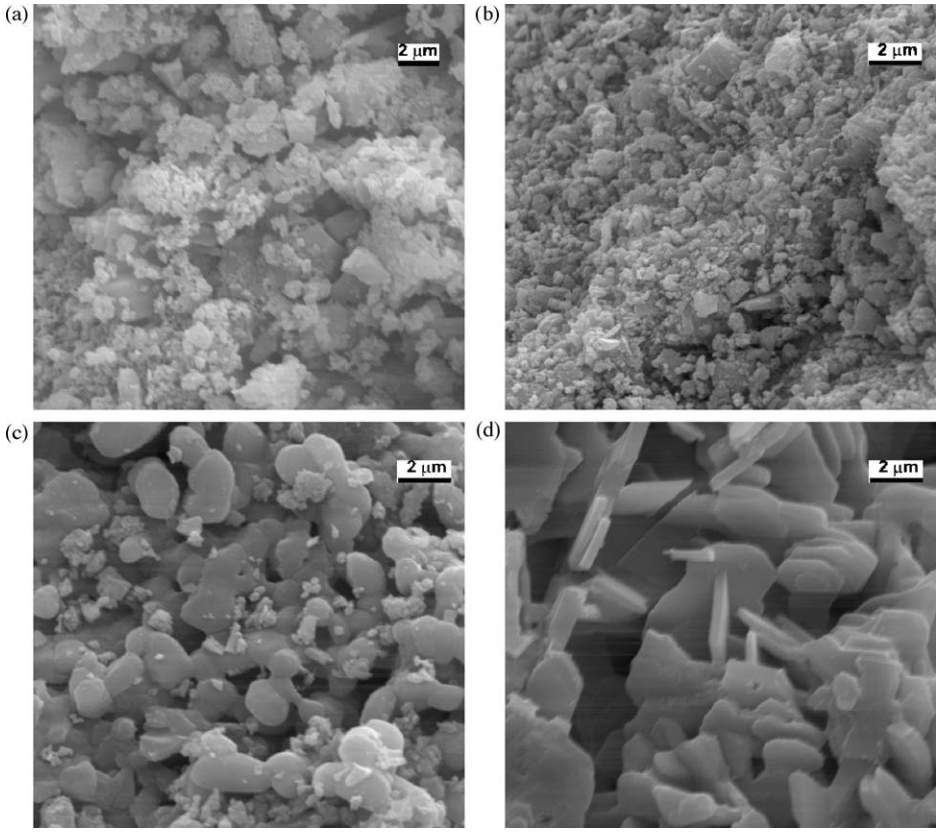

Fig. 8. SEM micrographs of samples of castable *A*, in a region of the matrix, treated at different temperatures: (a) dried at 110 °C, (b) 650 °C, (c) 1100 °C and (d) 1550 °C.

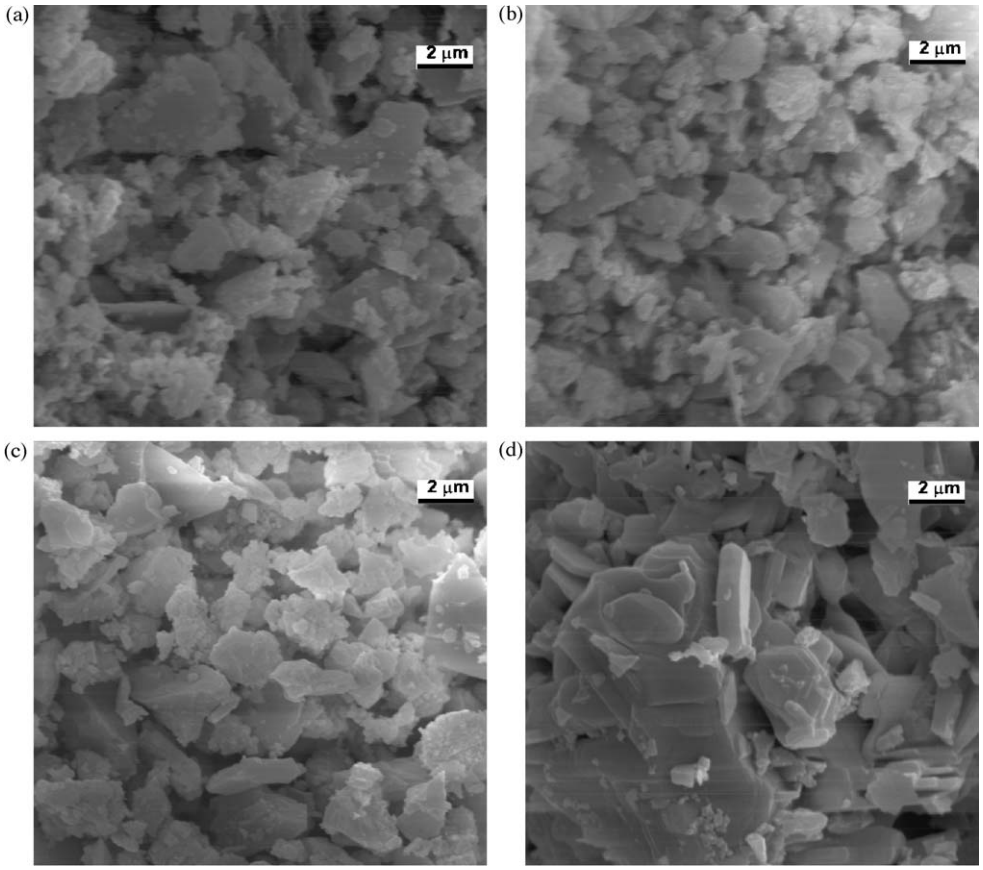

Fig. 9. SEM photomicrographs of samples of castable *B*, in a region of the matrix, treated at different temperatures: (a) dried at 110 °C, (b) 650 °C, (c) 1100 °C and (d) 1550 °C.

aggregates to each other. Because the test specimens were cured at 23 °C, the hydrates formed were probably AH_3 and CAH_{10}, which, after drying at 110 °C, the literature [4,10] and Fig. 3 suggest transformation into AH_3 and C_3AH_6. A comparison of the microstructures of the refractories indicates that material *A* has a finer hydrate structure than *B*. The microstructure, however, does not alter the maximum load behavior at lower treatment temperatures (see Fig. 7).

Consistent with the literature [4,10], the calcium and aluminum hydrates decompose at 650 °C, forming CA-type aluminates. The CA-type aluminates, together with remainder Al_2O_3, are the microstructures depicted in Figs. 8(b) and 9(b). These microstructures have finer particles than those of the solely dried material. Material strength decreased by 650 °C due to the decomposition of the hydrates in the samples. This explains the lower maximum load compared with that resulting from the treatment at 110 °C. The *B* refractory had a slightly smaller strength decrease than *A* at 650 °C (Fig. 7).

Figs. 8(c) and 9(c) show microstructures with a certain degree of sintering characterized by the formation of necks and the rounding of grain edges, which is very clearly visible in material *A*. This obviously leads to higher mechanical strength due to the greater cohesion of the system. According to the literature, this microstructure consists predominantly of α-Al_2O_3, CA and CA_2. In spit of lower densities and greater porosities for both refractories, the contribution of the ceramic bonds improved the mechanical strength when measured at room temperature.

The changes in the microstructures depicted in Figs. 8(c) and 9(c) can be compared with that presented in Fig. 2(a), that was taken from the work of J. M. Auvray et al. [2]. The effect of this microstructure is identified in Fig. 7 for both refractories treated at 1100 °C, with material *B* displaying significantly greater mechanical strength.

Treating refractories *A* and *B* at 1550 °C for 12 h led to major changes in their microstructures, which displayed well-defined morphologies and grain sizes in the matrix, as shown in Figs. 8(d) and 9(d). This morphology is characteristic of CA_6, and can be compared with that shown in Fig. 2(b). Moreover, this microstructure showed higher maximum load strength for both refractories, although refractory *B* displayed a greater difference than *A*. This greater difference is probably ascribable to matrix/aggregate interaction, since the aggregates in refractory *B* are much larger than those in refractory *A*. The large particle size distributions for castable *B* (Table 2), can help strength due to lower final porosity than castable *A* (Table 3), in spit of small difference between *A* and *B* castables porosities.

3.5. Fracture energy

Fig. 10 shows the results of fracture energy for the two refractories under study, obtained from the load–displacement

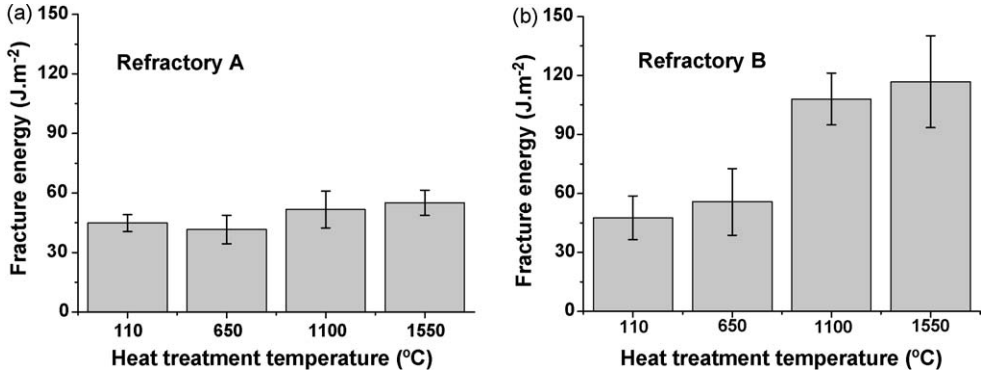

Fig. 10. Fracture energy results for the samples of refractory castables *A* and *B* heat-treated at the temperatures indicated under the horizontal axes.

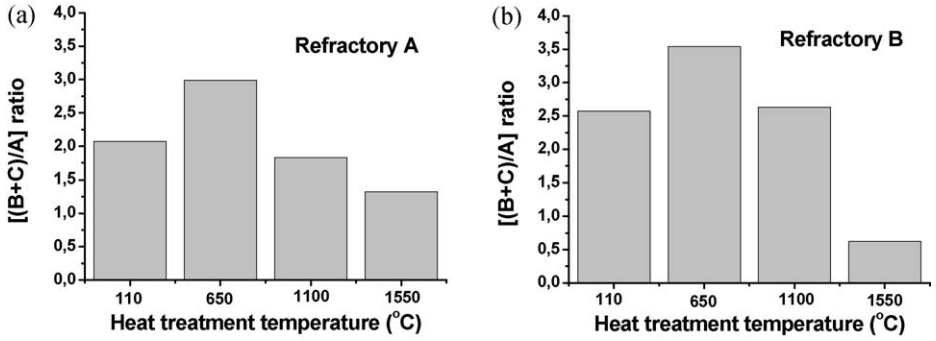

Fig. 11. Relative crack-propagation work: relation between $(B + C)$ work and purely elastic work, A, for refractories A (a), and B (b), treated at the temperatures indicated under the horizontal axes.

curves, fractured area and Eq. (3). In order to determine mean values, at least five distinct samples were used for each heat treatment temperature.

The behavior of the fracture energy of the analyzed refractories basically followed maximum load data in Fig. 7, i.e., a tendency to increase with increasing heat treatment temperatures, except at the temperature of 650 °C. Refractory *B*, however, behaved differently at 650 °C, displaying an increase in fracture energy in relation to the temperature of 110 °C, showing a slight increase. Note also, in Fig. 10, that castable *B* showed a significant increase in fracture energy in the test specimens treated at 1100 and 1550 °C, unlike refractory *A*, which showed a slight increase in fracture energy from 650 to 1100 and 1550 °C. In general, there is a good correlation between the maximum load behavior and the fracture energy as a function of the heat treatment temperature. Moreover, it is clear that the greater cohesion of the refractory castable matrix and the matrix–aggregate bond leads to higher values of maximum load and fracture energy. It appears that the difference in maximum load and fracture energy between *A* and *B* could be due to the hole of the size and particles size of the aggregates, see Table 2, in the castable *B*, which causes a significant increase in the fracture energy of the sintered materials.

3.6. Relative crack-propagation work

The $[(B + C)/A]$ ratio indicates the extent to which a material resists crack propagation after it initiates at the beginning of the curvature of the $P \times \delta$ curve. The higher this ratio, the greater the material's resistance to crack propagation. The graphs in Fig. 11 show the value of this ratio, determined from the integral under the load–displacement curve of the type shown in Fig. 4. Note that the behavior of the two refractories is similar, i.e., they display the same tendency with respect to the relative crack-propagation work. However, also note that, at all the temperatures applied in this study, refractory *A* shows lower values for the respective heat treatment temperatures than refractory *B*, except at 1550 °C. This indicates that refractory *B* is more resistant to crack

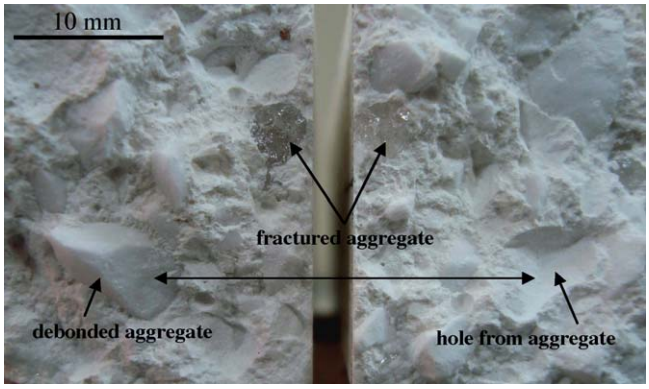

Fig. 12. Photograph of the fractured sample showing: matrix (fine fraction), fractured and debonded aggregates (coarse fraction), and hole produced by pull out of the aggregate.

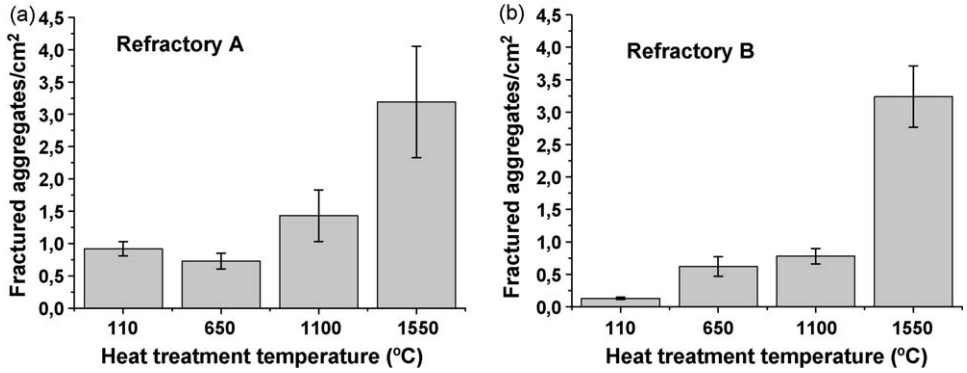

Fig. 13. Results of the count of fractured aggregates at the fracture surface, in the samples of refractories *A* (a) and *B* (b) heat-treated at the temperatures shown under the horizontal axes.

propagation than *A*, but when sintered at 1550 °C, this property decreases drastically in refractory *B*. The behavior of refractory *B* resulting from the treatment at 1550 °C indicates that most of the fracture energy (γ_{wof}) it has in relation to the other values shown in Fig. 10 is more a consequence of its high mechanical strength (high value of P_{max}) than because of some toughening process that may have caused a greater extension of the $P \times \delta$ curve. In contrast, Fig. 11 clearly shows that the relative crack-propagation work declined substantially in the material treated at 1550 °C, making it more brittle and less resistant to crack propagation.

Because the materials are very similar from the standpoint of chemical composition, it was concluded that these differences between materials *A* and *B* originate from the difference in the sizes of the largest aggregates in each material, but other mechanism may influence the crack propagation that need to study in the future, mainly at 1550 °C.

3.7. Aggregates behavior—fractured and non-fractured aggregates

Fig. 12 shows the fractured surface of the castables *B*, sintered at 1100 °C for 12 h, illustrating the fractured aggregates and debonded aggregates, and the place where the aggregates were debonded from the refractory castable matrix.

The question of the number of aggregates broken during fracturing, was counted, and the results of those counts in the test specimens after the stable crack propagation tests are shown in Fig. 13. The way this analysis was carried out allows only for a comparison of results of the samples of the same refractory at their respective heat treatment temperatures, not a comparison of the two refractories. The reason for this condition is that only the fractured aggregates were counted, and this number was divided by the fractured area of the test specimen. Refractory *A* has a larger number of smaller aggregates than refractory *B*. Due to the smaller size of aggregates in *A* sample, was impossible to count the total number of aggregates to find the percentage of this number. The typical values extracted from Fig. 13 for the materials treated at 1550 °C, for example, 3.3 aggregates/cm^2, are too distinct to be compared to the total number of large aggregates per unit of cross-section of each material.

An analysis of graphs (a) and (b) in Fig. 13 reveals that the number of fractured aggregates increased with the heat treatment temperature, indicating that the aggregates are strongly bonded in the structure of the matrix, and that the energy required to debond from the matrix would be higher than their resistance to fracture. This occurred in both *A* and *B* refractories of this study. This behavior is more pronounced for the higher test temperature at 1550 °C, when sintering occurred.

In both the refractories, it was also found that the greatest difference in the numbers of fractured aggregates occurred at the temperature of 1550 °C, which may be caused by the high degree of cohesion resulting from the sintering of the refractories, which was also reflected in the maximum load and the fracture energy.

The overall results of this research indicate that greater cohesion of large particles in the refractory matrix microstructure resulted from the increase in heat treatment temperature, which increased not only the fracture energy of these materials, but also the maximum load attained during stable crack propagation tests, and in the number of large particles of aggregates broken by the crack. However, the relative crack-propagation work, defined in this research by the $[(B + C)/A]$ ratio, showed a tendency to decline after reaching a maximum in the samples treated at 650 °C, demonstrating that these materials become more brittle with increasing temperature above 650 °C or tend to become unstable in slow crack propagation. This finding indicates that, in these materials, the increase in fracture energy was more due to the increase in the material's mechanical strength (greater cohesion of the system) than to the introduction of mechanisms that might have rendered the material more ''ductile'', in the sense that the test specimen could withstand larger openings of the crack before sample failure by crack propagation occurred. Thus, it can be stated that although the materials became stronger through better sintering and showed a higher fracture energy value, they nevertheless became more brittle, as indicated by the relative crack-propagation work.

4. Conclusions

The heat treatment temperature of the high alumina refractory castables of this study exerted a significant influence on the maximum load, fracture energy and matrix/aggregate cohesion. Heat treatment also impacted the number of fractured aggregates and the relative crack-propagation work. From this research, the following conclusions were reached:

1. The different microstructures of the two castables investigated as a function of the heat treatment temperature were determined to be responsible for the different levels of maximum load and fracture energy.
2. In general, there is a correlation between the maximum load and the fracture energy in the refractory castables studied.
3. The increase in the mechanical strength of these refractories caused the fracture energy to increase, although the materials became more brittle, as indicated by the lower relative crack-propagation work.
4. The main goal of this work was to show the behavior of refractories castable when subjected to different temperatures treatment, changes in properties were evaluated using maximum load, fracture energy and relative crack-propagation work as measured properties. The differences of some measured properties of the two castables can be correlation with different size and size distributions of the aggregates when the castables had similar chemical composition and cement content.

Acknowledgements

The authors gratefully acknowledge the financial support of this work by FAPESP (Fundação de Amparo à Pesquisa do Estado de São Paulo) through process #2001/04324-8; by CNPq (Conselho Nacional de Desenvolvimento Científico e Tecnológico) through a Research Productivity Grant, processes #304980/2003-0 and 301073/2006-6; and by the Universal Project through process #470504/2004-8 and a Senior Post-Doctoral fellowship, process #150038/2006-2. We are also indebted to CAPES for Procad project number 0136050 and for Probal project number 258/07.

References

[1] W.E. Lee, W. Vieira, S. Zhang, K. Ghanbari Ahari, H. Sarpoolaky, C. Parr, Castable refractory concretes, Int. Mater. Rev. 46 (2001) 145–167.
[2] J.M. Auvray, C. Gault, M. Huger, Evolution of elastic properties and microstructural changes versus temperature in bonding phases of alumina and alumina-magnesia refractory castable, J. Am. Ceram. Soc. 27 (2007) 3489–3496.
[3] J. Soro, A. Smith, C. Gault, Thermomechanical characteristics of calcium aluminate cement and sand tapes prepared by tape casting, J. Am. Ceram. Soc. 26 (2006) 3799–3807.
[4] F. Simonin, C. Olagnon, S. Maximilien, G. Fantozzi, Room temperature quasi-brittle behaviour of an aluminous refractory concrete after firing, J. Am. Ceram. Soc. 22 (2002) 165–172.
[5] F. Thummen, C. Olagnon, N. Godin, Cyclic fatigue and lifetime of a concrete refractory, J. Am. Ceram. Soc. 26 (2006) 3357–3363.
[6] J. Adachi, K. Kurosaki, M. Uno, S. Yamanaka, Porosity influence on the mechanical properties of polycrystalline zirconium nitride ceramics, J. Nucl. Mater. 358 (2006) 106–110.
[7] S. Giraud, J. Canel, Young's modulus of some SOFCs materials as a function of temperature, J. Am. Ceram. Soc. 28 (2008) 77–83.
[8] D. Lee, H. Choi, C. Han, H. Jeong, A compensation of Young's modulus in polysilicon structure with discontinuous material distribution, Matter Lett. 59 (2005) 3900–3903.
[9] S. Puchegger, F. Dose, D. Loidl, K. Kromp, R. Janssen, D. Brandhuber, N. Hüsing, H. Peterlik, The dependence of the elastic moduli of reaction bonded alumina on porosity, J. Am. Ceram. Soc. 27 (2007) 35–39.
[10] Alcoa Brochure: High Alumina Cements & Chemical Binders, 1996, 15 p.
[11] Y.C. Ko, Influence of the total fines content on the thermal shock damage resistance of Al_2O_3-spinel castables, Ceram. Int. 27 (2001) 501–507.
[12] D.P.H. Hasselman, Figures-of-merit for the thermal stress resistance of high-temperature brittle materials: a Review, Ceramurgia. Int. 4 (1978) 147–150.
[13] D.P.H. Hasselman, Elastic energy at fracture and surface energy as design criteria for thermal shock, J. Am. Ceram. Soc. 46 (11) (1963) 535–540.
[14] D.P.H. Hasselman, Unified theory of thermal shock fracture initiation and crack propagation in brittle ceramics, J. Am. Ceram. Soc. 52 (11) (1969) 600–604.
[15] D.R. Larson, J.A. Coppola, D.P.H. Hasselman, R.C. Bradt, Fracture toughness and spalling behavior of high-Al_2O_3 refractories, J. Am. Ceram. Soc. 57 (10) (1974) 417–421.
[16] B. Alapin, M. Ollig, J. Pötschke, Thermomechanical properties of selected refractory materials, in: Proceedings of 46th Inter. Coll. Refr. Eurogress Aachen, Germany, (2003), pp. 107–112.
[17] H. Harmuth, K. Rieder, M. Krobath, E. Tschegg, Investigation of the nonlinear fracture behaviour of ordinary ceramic refractory materials, Mater. Sci. Eng. A 214 (1996) 53–61.
[18] J.A. Rodrigues, V.C. Pandolfelli, Thermal treatment temperature and its influence on the thermal shock parameters of refractory castables, Interceram 51 (3) (2002) 186–189.
[19] J.A. Rodrigues, V.C. Pandolfelli, M. Rigaud, Elevated temperature thermal shock parameters for refractories, Interceram 51 (5) (2002) 322–326.
[20] S. Bueno, C. Baudin, Mechanical behaviour of structural ceramics, Bol. Soc. Esp. Ceram. 46 (2007) 103–118.
[21] H. Harmuth, Stability of crack propagation associated with fracture energy determined by wedge splitting specimen, Theor. Appl. Fract. Mech. 23 (1995) 103–108.
[22] A. Hillerborg, M. Modéer, P.E. Petersson, Analysis of crack formation and crack growth in concrete by means of fracture mechanics and finite elements, Cement Concrete Res. 6 (1976) 773–782.
[23] C. Rosselló, M. Elices, G.V. Guinea, Fracture of model concrete: fracture energy and characteristic length, Cement Concrete Res. 36 (2006) 1345–1353.
[24] Y. Kajita, S. Kariya, H. Kozuka, T. Holanda, S. Ota, Development a method for quantitative assessment of flexibility and its application for evaluating MgO–CaO–ZrO_2 bricks, in: Proceedings of UNITECR, 1997, pp. 337–345.
[25] K.-R. Wu, B. Chen, W. Yao, D. Shang, Effect of coarse aggregate type on mechanical properties of high-performance concrete, Cement Concrete Res. 31 (2001) 1421–1425.
[26] G.V. Guinea, K.E. Sayed, C.G. Rocco, M. Elices, J. Planas, The effect of the bond between the matrix and aggregates on the cracking mechanism and fracture parameters of concrete, Cement Concrete Res. 32 (2002) 1961–1970.
[27] T. Sadowski, G. Golewski, Effect of aggregate kind and graining on modelling of plain concrete under compression, Comput. Mater. Sci. 43 (2008) 119–126.
[28] T. Akçaoglu, M. Tokyay, T. Celik, Assessing the ITZ microcracking via scanning electron microscope and its effect on the failure behavior of concrete, Cement Concrete Res. 35 (2005) 358–363.
[29] E. Tschegg, Austrian Patent AT390328B, registered (1986).

[30] E. Brühwiler, F.H. Wittmann, The wedge splitting test, a new method of performing stable fracture mechanics tests, Eng. Fract. Mech. 35 (1990) 117–125.
[31] R. Nilica, H. Harmuth, Mechanical and fracture mechanical characterization of building materials used for external thermal insulation composite systems, Cement Concrete Res. 35 (2005) 1641–1645.
[32] S. Ribeiro, J.S.C. Vieira, C.C.D. Exposito, J.A. Rodrigues, in: Proceedings 10th Unified International Technical Conference on Refractories (UNITECR), Dresden, Alemanha, (2007), pp. 498–502.
[33] B. Trunk, G. Schober, A.K. Helbling, F.H. Wittmann, Fracture mechanics parameters of autoclaved aerated concrete, Cement Concrete Res. 29 (1999) 855–859.